Materials & Design 259 (2025) 114815

Contents lists available at ScienceDirect

Materials & Design

journal homepage: www.elsevier.com/locate/matdes

Design of novel non-periodic biomimetic bone scaffolds using the Moving Morphable Components method

Hao Wang [a,b], Jiongyi Wu [b], Yuhang Chen [c], Michael Zhuravkov [d], Sergei Bosiakov [d], Youwei Zhang [b], Mohammed Rafiq Abdul Kadir [e], Jian Jiang [a,**], Yongtao Lyu [a,b,f,*]

[a] Department of Spinal Surgery, Central Hospital of Dalian University of Technology, Dalian University of Technology, Dalian 116033, China
[b] Department of Engineering Mechanics, School of Mechanics and Aerospace Engineering, Dalian University of Technology, No. 2 Linggong Road, Dalian 116024, China
[c] School of Engineering and Physical Sciences, Heriot-Watt University, Edinburgh, UK
[d] Faculty of Mechanics and Mathematics, Belarusian State University, Minsk, Belarus
[e] Department of Biomedical Engineering, Faculty of Engineering, Universiti Malaya, 50603 Kuala Lumpur, Malaysia
[f] DUT-BSU Joint Institute, Dalian University of Technology, Dalian 116024, China

ARTICLE INFO

Keywords:
Bone scaffolds
Non-periodic structures
Biomimetic
Moving Morphable Components method
Topology optimization

ABSTRACT

Bone scaffolds are widely used in orthopedics for tissue repair and regeneration, yet achieving optimal bone growth through porous scaffolds remains a significant challenge. In this study, the Moving Morphable Components (MMC) method was employed to design novel non-periodic biomimetic bone scaffolds. Four types of scaffolds were created to mimic different human bone tissues. Their average elastic moduli were evaluated, and found to closely match with those of the corresponding bone tissues. Compared to triply periodic minimal surface (TPMS) structures, the novel scaffolds exhibited significantly higher permeability – up to 3.70×10^{-8} m^2 at a porosity of 62 %. These scaffolds demonstrated not only suitable mechanical properties but also enhanced permeability. Furthermore, they showed a good manufacturability, making them practical for fabrication. Overall, the MMC-designed scaffolds present a promising solution with matched mechanical properties and superior permeability, potentially reducing stress shielding and promoting bone cell growth and regeneration in tissue engineering applications.

1. Introduction

With the increasing prevalence of bone diseases and traumas worldwide, bone scaffolds have gained widespread applications in orthopedics for bone repair and regeneration [1,2]. Bone grafts are now the second most commonly transplanted tissue after blood transfusion, and are extensively used in trauma, orthopedics, and dental surgeries. However, current clinical treatments for bone defects, such as autologous bone grafts, allografts and synthetic implants, are limited by factors including insufficient tissue supply, immune rejection and foreign body response [1], and stress shielding resulting from suboptimal material and microstructural design. Consequently, effectively addressing bone defects remains a significant clinical challenge. Nonetheless, ongoing research and innovation in bone scaffold development hold promise in overcoming these limitations. With the ability to engineer scaffolds with tailored mechanical and biological properties, this field is rapidly evolving to meet growing clinical demands.

Most bone scaffolds are designed using conventional optimization algorithms and manufacturing techniques, typically resulting in structures based on the spatial arrangement of periodic or non-periodic unit cells. However, one major challenge in scaffold-based implants is stress shielding, which leads to implant loosening and bone resorption [3]. This phenomenon is primarily caused by the mismatch in mechanical properties between the scaffold and surrounding bone tissue, ultimately hindering effective tissue ingrowth and long-term implant stability [4]. To address this, scaffolds must be designed to transfer physiological loads effectively to the host bone, thereby mitigating stress shielding after implantation [5,6]. Ideally, scaffold structures should mimic the mechanical properties of human bone. Although porous microstructures formed from periodic arrays of unit cells can offer a balance between stiffness and permeability, they often fail to reproduce the anisotropic mechanical behavior characteristic of natural bone [7,8]. While triply

* Corresponding author at: Department of Engineering Mechanics, Dalian University of Technology, No.2 Linggong Road, Dalian 116024, China.
** Co-corresponding author.
E-mail addresses: rejustin@sina.com (J. Jiang), yongtaolu@dlut.edu.cn (Y. Lyu).

https://doi.org/10.1016/j.matdes.2025.114815
Received 22 July 2025; Received in revised form 2 September 2025; Accepted 22 September 2025
Available online 24 September 2025

periodic minimal surface (TPMS) structures offer favorable environments for bone cell growth and adequate mechanical support [9], they are limited in achieving directional anisotropy due to their inherently uniform unit cell patterns. Recent studies have explored geometric customization to introduce anisotropic properties. For instance, Wieding et al. [10] optimized strut diameters and placement in cubic, diagonal, and pyramidal scaffold architectures to match the mechanical performance of cortical bone, achieving location-specific mechanical properties. Similarly, Kong et al. [11] developed biomimetic scaffold structures that mimic several features of human trabecular bone. However, these approaches often involve time-consuming manual design processes and struggle to reproduce the complexity of real bone tissues. While Liu et al. [12,13] applied topology optimization to address mechanical performance, they neglected critical factors such as permeability and cell growth environments. Thus, despite improvements in certain properties, significant discrepancies still remain between the mechanical and biological performance of current scaffold designs and human bone.

Various methods have been employed to design bone scaffolds, with topology optimization proving particularly effective in generating optimal structural layouts with desirable properties. Among these, the Solid Isotropic Material with Penalization (SIMP) method has been widely used to create porous structures with graded porosity distributions, resembling the morphology and mechanical properties of cancellous bone [14]. However, despite its advantages, SIMP-based topology optimization often suffers from numerical issues such as tessellation artifacts, grid dependency, and the presence of grayscale elements, which can hinder manufacturability and model accuracy. The Voronoi Tessellation Method (VTM) offers an alternative by generating irregular porous structures that mimic the geometrical heterogeneity of natural bone [15]. Nevertheless, its irregularity introduces difficulties in establishing precise structure–property relationships, especially for complex functional requirements. More recently, machine learning approaches have been explored for the inverse design of anisotropic bone scaffolds [12,13,16], but their success is highly dependent on the quality and diversity of the training dataset. While these methods can generate non-periodic bone scaffold architectures, each comes with inherent limitations – whether computational, structural, or interpretability-related. Therefore, the efficient and accurate design of non-periodic biomimetic bone scaffolds that replicate the mechanical behavior of human bone remains a significant and ongoing challenge.

To overcome the limitations of existing scaffold design methods, novel approaches are required for the development of biomimetic bone scaffolds. One such promising technique is the Moving Morphable Components (MMC) method, first introduced by Guo and colleagues [17,18]. This topology optimization framework utilizes predefined components with variable geometries as the basic building blocks, enabling the construction of structures with diverse topologies. Unlike conventional methods, the MMC approach allows for continuous variation in component thickness and offers significantly improved computational efficiency and numerical stability. The versatility of the MMC method had led to its successful application across various fields of structural optimization. For instance, Rochefort-Beaudoin et al. [19] demonstrated the integration of a deep learning model to predict optimal MMC parameters, streamlining the design process. Zhou et al. [20] applied the MMC approach to optimize grid-reinforced plate structures under out-of-plane loading, while Tran et al. [21] enhanced the method by incorporating Bayesian optimization, addressing issues related to local optima and reducing the design space. Given its advantages in flexibility, stability and efficiency, the MMC method holds great potential for the design of non-periodic biomimetic bone scaffolds. Its ability to create structurally optimized, bone-like architectures is a compelling alternative to traditional scaffold design techniques.

In this study, the MMC method was applied to design bone scaffolds that exhibited both favorable mechanical performance and enhanced permeability – key factors for promoting bone tissue regeneration. An explicit boundary evolution technique was employed to optimize the porous scaffold layouts using the equivalent stiffness method. The designed scaffolds were evaluated in terms of effective elastic modulus, permeability, anisotropy, and manufacturability, demonstrating their potential to meet the functional requirements for bone defect repair. This investigation provides a promising framework and may inspire further research into the development of bone scaffolds with tailored, bone-mimicking properties.

2. Methodology

2.1. Theory of the MMC method

In this study, the pores within the structures are treated as fundamental components in the optimization process. The regions occupied by these pores are described using a topological description function (TDF), denoted as χ.

$$\begin{cases} \chi(x) > 0, \ \text{if } x \in \Omega, \\ \chi(x) = 0, \ \text{if } x \in \partial\Omega, \\ \chi(x) < 0, \ \text{if } x \in D\backslash(\Omega \cup \partial\Omega), \end{cases} \tag{1}$$

where D represents the prescribed design domain, Ω and $\partial\Omega$ represent the space occupied by the components and their boundaries, respectively.

As fundamental building blocks in topology optimization, the specific 3D structural components are mathematically represented using the TDF. The optimal layout is achieved by optimizing the parameters embedded within the TDF, such as the position, orientation, and geometry of each component. In this study, the TDF used to describe the cubic 3D structural components is defined as follows:

$$\chi(x,y,z) = 1 - \left(\frac{x'}{L_1}\right)^6 - \left(\frac{y'}{L_2}\right)^2 - \left(\frac{z'}{L_3}\right)^2 \tag{2}$$

with

$$\begin{Bmatrix} x' \\ y' \\ z' \end{Bmatrix} = \begin{bmatrix} R_{11}R_{12}R_{13} \\ R_{21}R_{22}R_{23} \\ R_{31}R_{32}R_{33} \end{bmatrix} \begin{Bmatrix} x - x_0 \\ y - y_0 \\ z - z_0 \end{Bmatrix} \tag{3}$$

and

$$\begin{bmatrix} R_{11} & R_{12} & R_{13} \\ R_{21} & R_{22} & R_{23} \\ R_{31} & R_{32} & R_{33} \end{bmatrix} = \begin{bmatrix} c_b c_t & -c_b s_t & s_b \\ s_a s_b c_t + c_a s_t & -s_a s_b s_t + c_a c_t & -s_a c_b \\ -c_a s_b c_t + s_a s_t & c_a s_b s_t + s_a c_t & c_a c_b \end{bmatrix} \tag{4}$$

where,-

$s_a = \sin\alpha, s_b = \sin\beta, s_t = \sin\theta, c_a = \sqrt{1-s_a^2}, c_b = \sqrt{1-s_b^2}$ and $c_t = \sqrt{1-s_t^2}$ with α, β, and θ denote the rotation angles of the component from a global coordinate system $O-x-y-z$ to the local coordinate system $O'-x'-y'-z'$ respectively, as shown in Fig. 1. The symbols x_0, y_0, z_0 denote the coordinates of the center point of the component, and L_1, L_2, andL_3 are used to represent the length, width, and height of the component, respectively.

To generate bending components, a trigonometric function was incorporated into the TDF in this study, as defined:

$$\chi(x,y,z) = 1 - \left(\frac{x'}{L_1}\right)^6 - \left(\frac{y' + \sin(x')}{L_2}\right)^2 - \left(\frac{z'}{L_3}\right)^2 \tag{5}$$

The TDF of the component is illustrated in Fig. 1. The design variables of a component are defined as $D^i = (x_0^i, y_0^i z_0^i, L_1^i, L_2^i, L_3^i, s_\alpha^i, s_\beta^i, s_\theta^i)$. Consequently, the topology of a porous structure can be uniquely represented and determined by a vector comprising the design variables of all components.

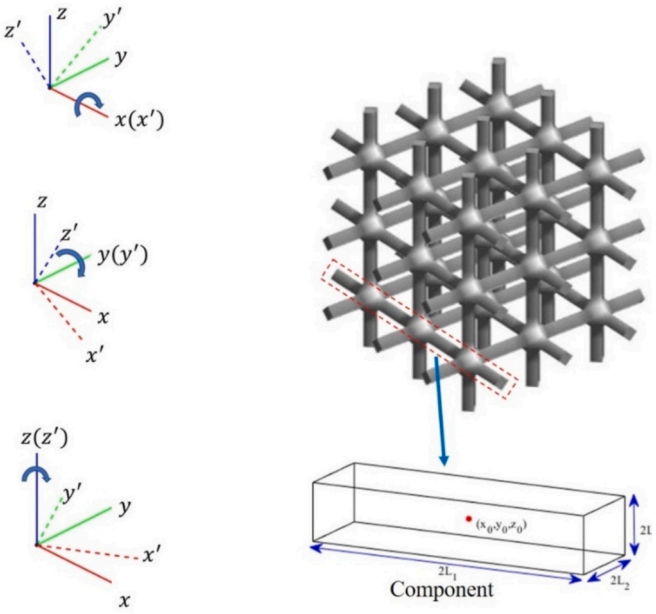

Fig. 1. Geometric description of pores.

2.2. Design of novel non-periodic biomimetic bone scaffolds using MMC

2.2.1. Design framework

After implantation, a bone scaffold serves not only as a mechanical support structure but also as a conducive environment for new tissue growth. Ideally, the scaffold should exhibit morphological and mechanical characteristics that closely resemble those of the host bone [22,23]. To calculate the Young's modulus and shear modulus in the objective function, various loading conditions were applied, with boundary conditions referenced from relevant literature [24,25], as illustrated in Fig. 2. Using the finite element (FE) method, the effective stiffness of the human bone was calculated from computed tomography (CT) images, as shown in Fig. 3. A 3D FE model was generated by converting the bone voxels into hexahedral elements [26]. Simulations were performed in Ansys (v18.0, Ansys Inc., Canonsburg, PA, United States), to assess compressive responses along the x, y and z axes, as well as shear behavior along the x-y, y-z and x-z planes. The stiffness matrix of the bone tissue was computed using a traditional homogenization approach based on Cauchy continuum theory [24,25]. Subsequently, orthogonal transformation was employed to derive the optimal representation of the stiffness matrix for each bone sample [27,16]. This process reduced the full stiffness matrix to nine independent constants, as the remaining components become negligibly small – rendering the approximation error minimal [27,12,13].

With the MMC-based topology optimization framework, the optimization problem was formulated as follows:

$$\begin{aligned} &\text{Find } D = \left(\left(\boldsymbol{D}^1\right)^\top, \cdots, \left(\boldsymbol{D}^i\right)^\top, \cdots, \left(\boldsymbol{D}^n\right)^\top\right)^\top \\ &\text{Minimize } I(\alpha_k) = \sum_{i,j=1}^{6} \left(\left(\boldsymbol{c}_{ij}^{\mathrm{H}} - \mathbf{c}_{ij}^{*}\right)/\mathbf{c}_{ij}^{*}\right)^2 \\ &\text{s.t.} \\ &\qquad K(D)u(D) = F, \\ &\qquad V(D) \le \overline{\boldsymbol{V}}, u = \overline{\boldsymbol{u}}, on\Gamma_u, D \subset \mathscr{U}_{\boldsymbol{D}}, \end{aligned} \tag{6}$$

where, the elastic tensor $\boldsymbol{c}$ with superscript '*' represents the target stiffness, and the tensor with superscript 'H' represents the stiffness of bone scaffold. $\boldsymbol{D}$ denotes the vector of design variables, and n represents the total number of pores. I is the objective function, symbol $\boldsymbol{u}$ represents the vector of structural displacement, $\boldsymbol{F}$ is the vector of equivalent external load, $\boldsymbol{K}$ is the global stiffness matrix, $\boldsymbol{V}(\boldsymbol{D})$ represents the volume ratio of the structure to be optimized, and $\overline{\boldsymbol{V}}$ is defined by the designer as the volume fraction, representing the upper limit of available solid material volume. $\overline{\boldsymbol{u}}$ is the displacement vector prescribed on the Dirichlet boundary Γ, and $\mathscr{U}_{\boldsymbol{D}}$ is the admissible sets for $\boldsymbol{D}$.

2.2.2. Structural connectivity

Structural connectivity is a critical attribute of bone scaffolds, as it plays a pivotal in supporting bone tissue ingrowth, vascularization, and efficient nutrient transport. In this study, the components in the MMC method were specifically tailored to ensure connectivity within the

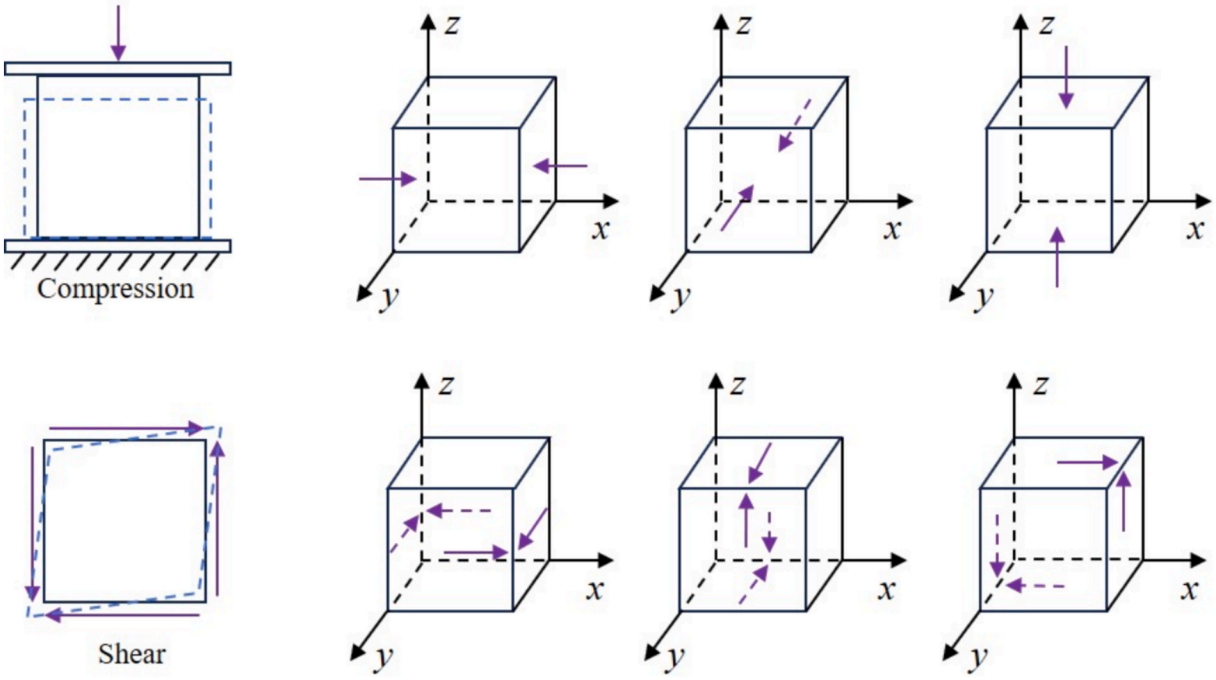

Fig. 2. The Young's moduli and shear moduli of the structure was calculated in the six loading conditions.

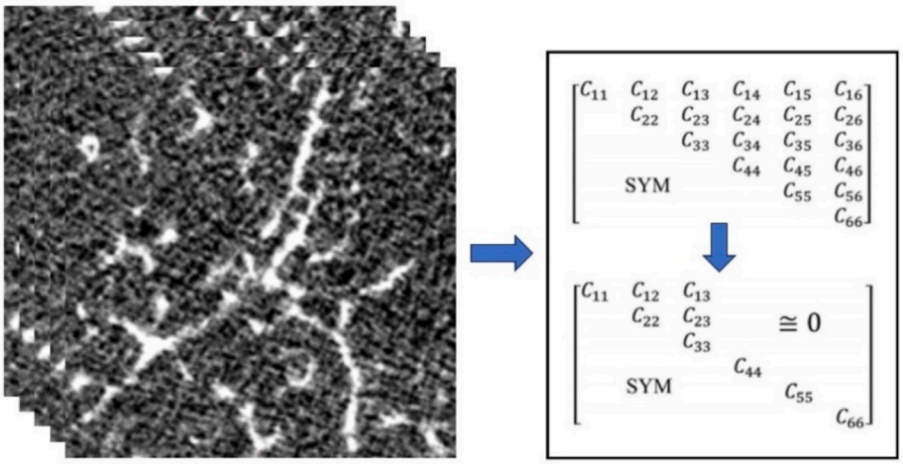

Fig. 3. CT images of vertebral cancellous bone and its stiffness matrix.

porous scaffold structure, with preforming components representing void regions and non-components area representing solid material. To satisfy the connectivity requirements, only scaffold components that connect specific regions, such as opposite surfaces, were considered during the design process. For simplicity, the design domain was defined as a cube with three sets of opposite faces. Special attention was given to connecting the top and bottom surfaces, which are essential for ensuring continuous load transfer and biological interaction. To enhance the likelihood of achieving such connections during the optimization process, the MMC components were allowed to scale and rotate within the design domain. Additionally, the component length was set to match the diagonal length of the cube, approximately 1.73 times the edge length, to increase the probability of spanning between opposite surfaces. To further prevent discounted or misaligned components, a minimum angle of 35.24° relative to the base was enforced. This configuration helps maintain functional connectivity across the scaffold while minimizing isolated solid regions.

2.2.3. Sensitivity analysis

In a gradient-based optimization algorithm, sensitivity information is provided to the minimization routine to guide the search toward the minimum value of the objective function along the most efficient path. Using $\alpha_k \in \boldsymbol{D}$ to denote any of the design variables in Eq. (6), the corresponding sensitivity derivation was given as $I_1 = \left(\left(\boldsymbol{c}_{11}^{\mathrm{H}} - \mathbf{c}_{11}^{*}\right)/\mathbf{c}_{11}^{*}\right)^2$ as an example. In I_1, only $\boldsymbol{c}_{11}^{\mathrm{H}}$ was related to the design variables, so only $\partial \boldsymbol{c}_{11}^{\mathrm{H}}/\partial \alpha_k$ was required.

$$\boldsymbol{c}_{11}^{\mathrm{H}} = \frac{\sigma_x}{\varepsilon_x} \tag{7}$$

where $\varepsilon_x = -0.1$ was applied as a displacement on one side of the cubic structure. Therefore, the magnitude of displacement in the x direction was set for each node as:

$$\boldsymbol{u}_R^x = -0.1 l \boldsymbol{E}_R^x \tag{8}$$

In the equation, $\boldsymbol{u}_R^x$ contains the degrees of freedom in the x direction for the nodes on that side. L represents the length and width of the computational model. $\boldsymbol{E}_R^x = [1, 1, 1, \cdots, 1]^\top$ represents a column vector of the same dimension as $\boldsymbol{u}_R^x$.

All other boundary nodes were fully constrained with zero displacement, i.e., $\boldsymbol{u}_L^x = \boldsymbol{u}_L^y = \boldsymbol{u}_L^z = \boldsymbol{u}_U^z = \boldsymbol{u}_D^z = \boldsymbol{u}_F^y = \boldsymbol{u}_B^y = 0$. The subscripts denote the directions of up, down, left, right, front, and back, and the superscripts indicate the displacement directions (x, y, or z). Substituting the known displacements boundary conditions and external loads, the block system of equations can be expressed as:

$$\begin{bmatrix} \boldsymbol{K}_{II} & \boldsymbol{K}_{IU}^z & \boldsymbol{K}_{ID}^z & \boldsymbol{K}_{IF}^y & \boldsymbol{K}_{IB}^y & \boldsymbol{K}_{IL}^x & \boldsymbol{K}_{IL}^y & \boldsymbol{K}_{IL}^z & \boldsymbol{K}_{IR}^x \\ \boldsymbol{K}_{UI}^z & \boldsymbol{K}_{UU}^{zz} & \boldsymbol{K}_{UD}^{zz} & \boldsymbol{K}_{UF}^{zy} & \boldsymbol{K}_{UB}^{zy} & \boldsymbol{K}_{UL}^{zx} & \boldsymbol{K}_{UL}^{zy} & \boldsymbol{K}_{UL}^{zz} & \boldsymbol{K}_{UR}^{zx} \\ \boldsymbol{K}_{DI}^z & \boldsymbol{K}_{DU}^{zz} & \boldsymbol{K}_{DD}^{zz} & \boldsymbol{K}_{DF}^{zy} & \boldsymbol{K}_{DB}^{zy} & \boldsymbol{K}_{DL}^{zx} & \boldsymbol{K}_{DL}^{zy} & \boldsymbol{K}_{DL}^{zz} & \boldsymbol{K}_{DR}^{zx} \\ \boldsymbol{K}_{FI}^y & \boldsymbol{K}_{FU}^{yz} & \boldsymbol{K}_{FD}^{yz} & \boldsymbol{K}_{FF}^{yy} & \boldsymbol{K}_{FB}^{yy} & \boldsymbol{K}_{FL}^{yx} & \boldsymbol{K}_{FL}^{yy} & \boldsymbol{K}_{FL}^{yz} & \boldsymbol{K}_{FR}^{yx} \\ \boldsymbol{K}_{BI}^y & \boldsymbol{K}_{BU}^{yz} & \boldsymbol{K}_{BD}^{yz} & \boldsymbol{K}_{BF}^{yy} & \boldsymbol{K}_{BB}^{yy} & \boldsymbol{K}_{BL}^{yx} & \boldsymbol{K}_{BL}^{yy} & \boldsymbol{K}_{BL}^{yz} & \boldsymbol{K}_{BR}^{yx} \\ \boldsymbol{K}_{LI}^x & \boldsymbol{K}_{LU}^{xz} & \boldsymbol{K}_{LD}^{xz} & \boldsymbol{K}_{LF}^{xy} & \boldsymbol{K}_{LB}^{xy} & \boldsymbol{K}_{LL}^{xx} & \boldsymbol{K}_{LL}^{xy} & \boldsymbol{K}_{LL}^{xz} & \boldsymbol{K}_{LR}^{xx} \\ \boldsymbol{K}_{LI}^y & \boldsymbol{K}_{LU}^{yz} & \boldsymbol{K}_{LD}^{yz} & \boldsymbol{K}_{LF}^{yy} & \boldsymbol{K}_{LB}^{yy} & \boldsymbol{K}_{LL}^{yx} & \boldsymbol{K}_{LL}^{yy} & \boldsymbol{K}_{LL}^{yz} & \boldsymbol{K}_{LR}^{yx} \\ \boldsymbol{K}_{LI}^z & \boldsymbol{K}_{LU}^{zz} & \boldsymbol{K}_{LD}^{zz} & \boldsymbol{K}_{LF}^{zy} & \boldsymbol{K}_{LB}^{zy} & \boldsymbol{K}_{LL}^{zx} & \boldsymbol{K}_{LL}^{zy} & \boldsymbol{K}_{LL}^{zz} & \boldsymbol{K}_{LR}^{zx} \\ \boldsymbol{K}_{RI}^x & \boldsymbol{K}_{RU}^{xz} & \boldsymbol{K}_{RD}^{xz} & \boldsymbol{K}_{RF}^{xy} & \boldsymbol{K}_{RB}^{xy} & \boldsymbol{K}_{RL}^{xx} & \boldsymbol{K}_{RL}^{xy} & \boldsymbol{K}_{RL}^{xz} & \boldsymbol{K}_{RR}^{xx} \end{bmatrix} \begin{Bmatrix} \boldsymbol{u}_I \\ 0 \\ 0 \\ 0 \\ 0 \\ 0 \\ 0 \\ 0 \\ -0.1 l \boldsymbol{E}_R^x \end{Bmatrix} = \begin{Bmatrix} 0 \\ \boldsymbol{f}_U^z \\ \boldsymbol{f}_D^z \\ \boldsymbol{f}_F^y \\ \boldsymbol{f}_B^y \\ \boldsymbol{f}_L^x \\ \boldsymbol{f}_L^y \\ \boldsymbol{f}_L^z \\ \boldsymbol{f}_R^x \end{Bmatrix} \# \tag{9}$$

where $\boldsymbol{u}_I$ denotes the free degrees of freedom, and the rest are either zero or prescribed. From Eq. (9), $\boldsymbol{u}_I$ and $\boldsymbol{f}_L^x$ can be solved. The stress in x-direction is defined as:

$$\sigma_x = \frac{\sum \boldsymbol{f}_L^x}{l} = \frac{1}{l}\left(\boldsymbol{E}_L^x\right)^\top \boldsymbol{f}_L^x \tag{10}$$

In Eq. (10), $\boldsymbol{E}_L^x = [1, 1, 1, \cdots, 1]^\top$ is a column vector of the same dimension as $\boldsymbol{f}_L^x$. Therefore, the sensitivity of the homogenized elastic constant is given by:

$$\frac{\partial \boldsymbol{c}_{11}^{\mathrm{H}}}{\partial \alpha_k} = \frac{1}{\varepsilon_x}\frac{\partial \sigma_x}{\partial \alpha_k} = \frac{1}{\varepsilon_x l}\left(\boldsymbol{E}_L^x\right)^\top \frac{\partial \boldsymbol{f}_L^x}{\partial \alpha_k} \tag{11}$$

From the block form of the global stiffness matrix, the following expressions hold:

$$\begin{aligned} \boldsymbol{K}_{LI}^x &= \left(\boldsymbol{Q}_L^x\right)^\top \boldsymbol{K} \boldsymbol{Q}_I \quad ; \quad \boldsymbol{K}_{LR}^{xx} = \left(\boldsymbol{Q}_L^x\right)^\top \boldsymbol{K} \boldsymbol{Q}_R^x \\ \boldsymbol{K}_{II} &= \left(\boldsymbol{Q}_I\right)^\top \boldsymbol{K} \boldsymbol{Q}_I \quad ; \quad \boldsymbol{K}_{IR}^x = \left(\boldsymbol{Q}_I\right)^\top \boldsymbol{K} \boldsymbol{Q}_R^x \end{aligned} \tag{12}$$

where:

$$\begin{aligned} \boldsymbol{Q}_L^x &= [\,0 \;\; 0 \;\; 0 \;\; 0 \;\; 0 \;\; \boldsymbol{I}_L^x \;\; 0 \;\; 0 \;\; 0\,]^\top \\ \boldsymbol{Q}_I &= [\,\boldsymbol{I}_I \;\; 0 \;\; 0 \;\; 0 \;\; 0 \;\; 0 \;\; 0 \;\; 0 \;\; 0\,]^\top \\ \boldsymbol{Q}_R^x &= [\,0 \;\; 0 \;\; 0 \;\; 0 \;\; 0 \;\; 0 \;\; 0 \;\; 0 \;\; \boldsymbol{I}_R^x\,]^\top \end{aligned} \tag{13}$$

From Eq. (9), the following equations can be obtained:

$$\frac{\partial \boldsymbol{f}_L^x}{\partial \alpha_k} = \left(\boldsymbol{Q}_L^x\right)^\top \frac{\partial \boldsymbol{K}}{\partial \alpha_k}\boldsymbol{Q}_I \boldsymbol{u}_I + \boldsymbol{K}_{LI}^x \frac{\partial \boldsymbol{u}_I}{\partial \alpha_k} - 0.1l\left(\boldsymbol{Q}_L^x\right)^\top \frac{\partial \boldsymbol{K}}{\partial \alpha_k}\boldsymbol{Q}_R^x \boldsymbol{E}_R^x \tag{14}$$

$$\frac{\partial \boldsymbol{u}_I}{\partial \alpha_k} = 0.1l\boldsymbol{K}_{II}^{-1}\left(\boldsymbol{Q}_I\right)^\top \frac{\partial \boldsymbol{K}}{\partial \alpha_k}\boldsymbol{Q}_R^x \boldsymbol{E}_R^x - \boldsymbol{K}_{II}^{-1}\left(\boldsymbol{Q}_I\right)^\top \frac{\partial \boldsymbol{K}}{\partial \alpha_k}\boldsymbol{Q}_I \boldsymbol{u}_I \tag{15}$$

Substituting Eqs. (14) and (15) into Eq. (11), the final sensitivity expression is:

$$\begin{aligned}\frac{\partial \boldsymbol{c}_{11}^{\mathrm{H}}}{\partial \alpha_k} = \frac{1}{\varepsilon_x l}\Bigg(&\left(\boldsymbol{Q}_L^x \boldsymbol{E}_L^x\right)^{\mathrm{T}} \frac{\partial \boldsymbol{K}}{\partial \alpha_k}\boldsymbol{Q}_I \boldsymbol{u}_I + 0.1l\left(\boldsymbol{E}_L^x\right)^{\mathrm{T}} \boldsymbol{K}_{LI}^x \boldsymbol{K}_{II}^{-1}\left(\boldsymbol{Q}_I\right)^{\mathrm{T}} \frac{\partial \boldsymbol{K}}{\partial \alpha_k}\boldsymbol{Q}_R^x \boldsymbol{E}_R^x - \\ &\left(\boldsymbol{E}_L^x\right)^{\mathrm{T}} \boldsymbol{K}_{LI}^x \boldsymbol{K}_{II}^{-1}\left(\boldsymbol{Q}_I\right)^{\mathrm{T}} \frac{\partial \boldsymbol{K}}{\partial \alpha_k}\boldsymbol{Q}_I \boldsymbol{u}_I - 0.1l\left(\boldsymbol{Q}_L^x \boldsymbol{E}_L^x\right)^{\mathrm{T}} \frac{\partial \boldsymbol{K}}{\partial \alpha_k}\boldsymbol{Q}_R^x \boldsymbol{E}_R^x\Bigg)\end{aligned} \tag{16}$$

The derivation of the remaining components for the sensitivity of the objective function follows a similar process and is thus omitted for brevity. It is important to note that, for computational efficiency, the term $\Delta \boldsymbol{K}/\Delta\alpha_k$, and the value of $\partial \boldsymbol{K}/\partial\alpha_k$ was approximated using the finite difference method in MATLAB (v2020b, MathWorks Inc., Natick, Massachusetts, USA) (i.e., $\partial \boldsymbol{K}/\partial\alpha_k \approx \Delta \boldsymbol{K}/\Delta\alpha_k$). This approximation method has been validated through numerical examples and demonstrated to be both effective and reliable. For a detailed derivation of $\partial \boldsymbol{K}/\partial\alpha_k$, readers are referred to the relevant work in the literature [28].

In this study, the primary constraint considered was the volume constraint. Accordingly, the sensitivity of the constraint in Eq. (6) can be expressed as:

$$\frac{\partial V}{\partial \alpha_k} = -\int_{\mathrm{D}} \delta^i(\chi^s)\mathrm{X}^i \mathrm{dV} \tag{17}$$

where δ represents the Dirac delta function, and $\delta^i(\chi^s) = \min(\delta(\chi_i), \delta(\chi^s)), i = 1, ..., n.\delta^i(\chi^s(x)) \neq 0$ was applied only to $x \in \partial\Omega_i \cap \partial\Omega_s$. In this case, the variation of each component of χ_i with respect to $\left(x_0, y_0, z_0, L_2, L_3, s_a, s_b, s_t\right)^\top$ can be computed as:

$$\begin{aligned}\Delta\chi_i = &A^i\Delta x_0^i + B^i\Delta y_0^i + C^i\Delta z_0^i + D^i\Delta L_2^i + E^i\Delta L_3^i \\ &+F^i\Delta s_a^i + G^i\Delta s_b^i + H^i\Delta s_t^i, i = 1, \cdots, n.\end{aligned} \tag{18}$$

where the values of A^i, B^i, C^i, D^i, E^i, F^i, G^i, and H^i can be found in the relevant work of Zhang et al. [29].

2.2.4. Generation of bone scaffolds

In this section, the geometric models of novel bone scaffolds were designed using the MMC method to match the properties of different human bone tissues. The geometric configuration and material characteristics of the initial structure are described below. Each scaffold was modeled as a cube with dimensions of 10.0 mm × 10.0 mm × 10.0 mm,

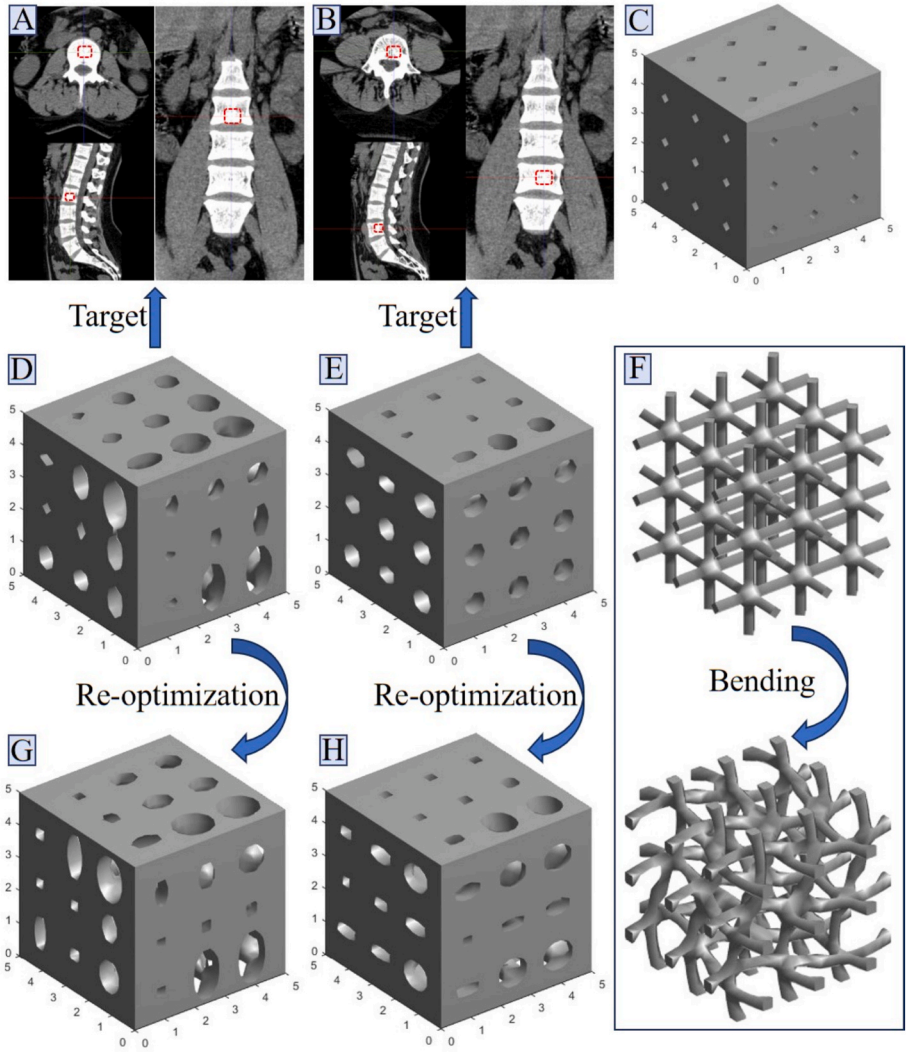

Fig. 4. Design process of the novel non-periodic biomimetic bone scaffolds. CT images (A) and (B) of bones were from different regions of the spine, respectively. (C) A cube with initial generated pores. (D) Straight pore type I. (E) Straight pore type II. (F) Transformation process from straight to bending pores. (G) Bending pore type I. (H) Bending pore type II.

containing internally generated pores, as illustrated in Fig. 4C. To balance design quality and computational efficiency, the number of components (or pores) per direction was set to 3 × 3, resulting in a total of 9 components. Increasing the number of components (e.g., 4 × 4) would significantly raise computational cost, while using fewer components (e.g., 2 × 2) would lead to suboptimal structural performance. The scaffold material was assumed to be isotropic, with a Young's modulus of 2500.0 MPa and a Poisson's ratio of 0.3. The structure was discretized using 20 × 20 × 20 eight-node hexahedral finite elements for numerical analysis.

To validate the feasibility of the novel biomimetic bone scaffolds designed using the MMC method, two distinct regions of human spinal bone were selected as target structures, as illustrated in Fig. 4A and B. The elasticity matrices of porous bone samples, computed using FE models, were employed as the target stiffness values for scaffold optimization. To calculate the effective modulus of these samples, a previously established method was adopted to generate heterogeneous FE models based on human bone data [26]. Initially, the scaffolds were optimized using straight components, resulting in designs with straight pore channels. Subsequently, efforts were made to transform these components into curved geometries in order to closely mimic the natural architecture of cancellous bones, as depicted in Fig. 4F. A trigonometric function was incorporated into the TDF, which can transform the straight components into the bending components. In addition to these types of components, other types of components can also be generated by incorporating different functions into the TDF. Although the straight and bending components were studied in this work, other types of components also deserved to be investigated in future works. Compared to straight pores, bending pores better resemble the irregular and interconnected morphology of human cancellous bones [30]. Accordingly, the components were re-optimized to produce scaffolds with bending pores, aiming to improve anatomical realism and biomechanical performance.

2.3. Evaluation on the performance of the novel bone scaffolds

2.3.1. Analysis of mechanical performance

The mechanical performance of the novel bone scaffolds was analyzed using the FE method. The structure of cancellous bone exhibits orthotropic characteristics, defined by three symmetric planes and nine independent elastic constants. To simplify the optimization process, scaffold design is typically reduced to the optimization of three Young's moduli and three shear moduli along principal directions in an orthotropic framework [23,31]. It is important to note that different initial design configurations can lead to distinct scaffold geometries, due to the presence of local optima and the existence of multiple valid solutions in topology optimization processes [32,33].

To improve modeling efficiency and avoid repeated mesh partitioning during the optimization process, a surrogate material FE model was employed. The design domain was discretized using eight-node hexahedral elements, and the material properties of each element were determined by mapping the structural components, representing regions not occupied by material, onto a fixed Eulerian grid [31]. Accordingly, the Young's modulus E_e^i for each element was calculated based on the material distribution as follows:

$$E_e^i = \frac{1}{8}\sum_{j=1}^{8}\left(H\left(\chi_j^e\right)\right)^q E^i \tag{19}$$

where E^i represents the Young's modulus of the material, $\chi_j^e (j = 1, \cdots, 8)$ are the values of the structural TDF $\chi^2(x)$ at the 8 nodes of element e, and q is an integer with $q = 2$.

The elastic modulus of each element was determined based on the known TDF values at its nodes. To distinguish between material and void regions, the Heaviside function, denoted as $H(x)$, was introduced. This function takes a value of 1.0 when $x \geq 0.0$, and 0.0 when $x \leq 0.0$. During the optimization process, a regularized form of the Heaviside function was employed to ensure numerical stability and differentiability. The regularized function is defined as follow:

$$H(x) = \begin{cases} 1, x > \varepsilon \\ \frac{3(1-\alpha)}{4}\left(\frac{x}{\varepsilon} - \frac{x^3}{3\varepsilon^3}\right) + \frac{1+\alpha}{2}, -\varepsilon \leq x \leq \varepsilon \\ \alpha, x < -\varepsilon \end{cases} \tag{20}$$

where the parameter ε controls the width of the transition region in the function, and the parameter α is introduced to avoid singularities in the stiffness matrix of the structure. Both parameters are small positive constants selected to ensure numerical stability during the optimization process.

2.3.2. Analysis of permeability

The permeability of the novel biomimetic bone scaffolds was evaluated using computational fluid dynamics (CFD) analysis. Mass transport behavior is a critical characteristic of bone scaffolds, as a high capacity for fluid is essential to support cell viability, nutrient delivery, and waste removal, thereby ensuring normal tissue growth. Given that the permeability of cancellous bone is predominantly oriented along the longitudinal direction of the body [34], this study focused exclusively on evaluating permeability in that direction. Simulations were conducted using COMSOL Multiphysics (v6.0, COMSOL Inc., Stockholm, Sweden), to model fluid flow through the scaffold structures and assess their effectiveness in facilitating mass transport.

The permeability of all four novel biomimetic bone scaffolds, each with dimensions of 10.0 mm × 10.0 mm × 10.0 mm was evaluated. It is worth noting that TPMS structures are widely used in bone scaffold design due to their favorable mechanical and transport properties, particularly in their high permeability [35]. Among these, the Schwarz P structure is recognized for its superior permeability performance. Therefore, in this study, the permeability of the novel scaffolds was compared with that of a Schwarz P scaffold. configured with a 3 × 3 × 3 unit cell array within the same overall dimensions, as shown in Fig. 5A. To simulate fluid flow through the scaffolds, a virtual fluid domain measuring 10.0 mm × 10.0 mm × 2.5 mm was added to both the top and bottom surfaces of each scaffold, as shown in Fig. 5B. The top surface of the model served as the fluid inlet, with a prescribed flow velocity of 0.001 m/s, while the bottom surfaces acted as the fluid outlet, with a fixed pressure of 0.0 Pa. All remaining surfaces were assigned no-slip wall boundary conditions. The permeability was then calculated based on the simulated results using Darcy's law, given by:

$$R_e = \frac{v\rho d}{\mu} \tag{21}$$

where R_e is the Reynolds number, v is the flow velocity, (ρ is the density of the fluid, d is the diameter of pores, and μ is the dynamic viscosity of the fluid.

The permeability of the scaffolds can be calculated as:

$$K = \frac{v\mu L}{\Delta P} \tag{22}$$

$$v = \frac{Q}{A} \tag{23}$$

where K is the permeability, L is the length of flow path, ΔP is the pressure drop, Q is the fluid flow, and A is the cross-section area of the fluid domain. The fluid was modeled as water with $\rho = 1000.0\ \mathrm{kg/m^3}$, μ

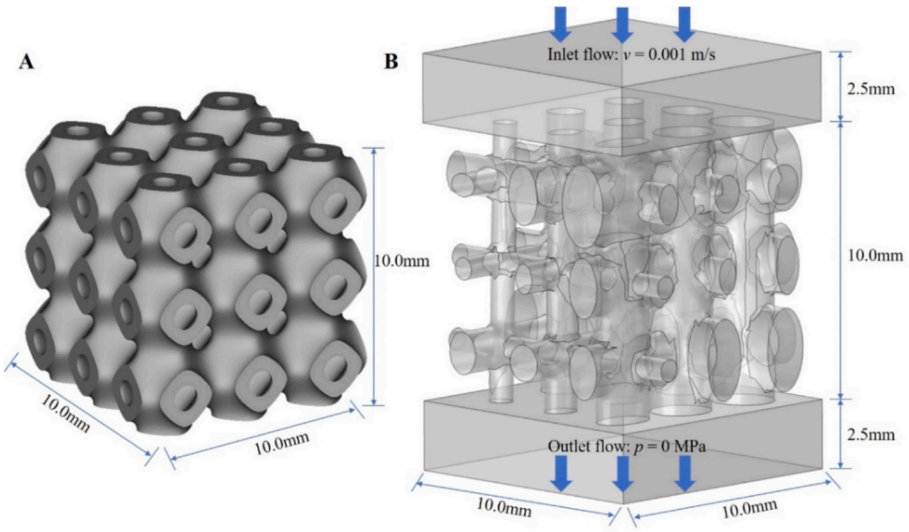

Fig. 5. Schematic diagrams of (A) Schwarz P scaffold structure and (B) fluid domain and boundary conditions of straight pore type I scaffold applied in the CFD simulation.

= 0.001 Pa•s, and v = 0.001 m/s. The fluid properties and flow conditions employed in this study are consistent with those used in previous research [28,36].

2.3.3. *Additive manufacturing*

In this study, the manufacturability of the novel biomimetic bone scaffolds was evaluated through additive manufacturing. The scaffolds were fabricated using the selective laser melting (SLM) technique with stainless steel 316L powder, in a 99.99 % argon atmosphere using an SLM machine (Renishaw AM400, Wotton-under-Edge, UK). The fabrication was carried out with a laser power of 160.0 W, scanning speed of 1000.0 mm/s, hatch spacing of 80.0μ m, and layer thickness of 30.0μ m. A bidirectional orthogonal scanning strategy was applied for each layer to ensure uniformity and structural integrity. To assess the quality of the printed scaffolds, a scanning electron microscope (SEM) was used to examine their surface morphology and fidelity to the original design, thereby verifying the manufacturability of the novel biomimetic structures.

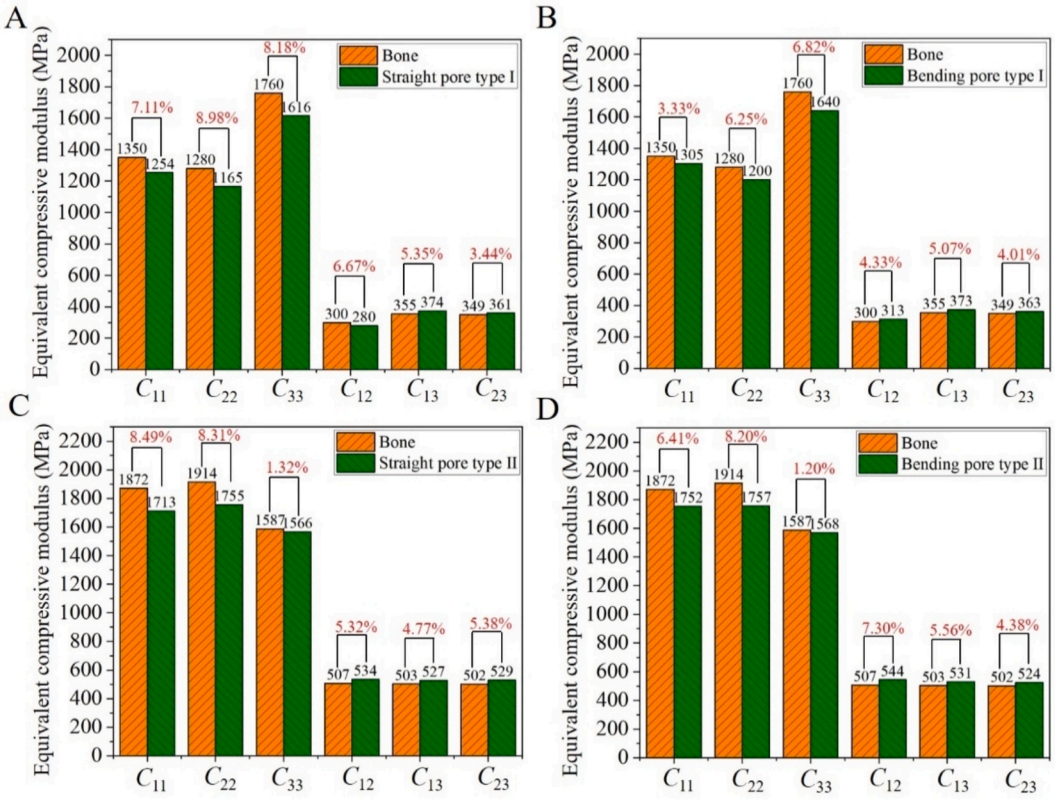

Fig. 6. Comparison of the anisotropic elastic properties of the designed non-periodic biomimetic bone scaffolds with those of human cancellous bone. (A) Bone scaffold with straight pore type I. (B) Bone scaffold with straight pore type II. (C) Bone scaffold with bending pore type I. (D) Bone scaffold with bending pore type II.

3. Results

3.1. Geometric model of bone scaffolds

Using the porous bone tissue shown in Fig. 4A as the target stiffness, a bone scaffold with straight pore type I was design with a porosity of 62 %, as shown in Fig. 4D. Similarly, based on the bone tissue in Fig. 4B, a bone scaffold with straight pore type II with a porosity of 67 % was obtained, as shown in Fig. 4E. These initial scaffold structures (Fig. 4D and E) were subsequently adjusted and re-optimized using curved components to better mimic the target bone tissues. The same bone samples from Fig. 4A and B were used as target stiffnesses. As a result, two biomimetic bone scaffolds with bending pores were developed. The bending pore type I scaffold, with a porosity of 62 % is shown in Fig. 4G, while the bending pore type II scaffold, with a porosity of 67 %, is shown in Fig. 4H.

3.2. Mechanical properties of bone scaffolds

The novel non-periodic biomimetic bone scaffolds were designed to satisfy mechanical behavior requirements by closely matching the anisotropic mechanical properties of human cancellous bone. Due to its naturally irregular porous architecture, cancellous bone exhibits inherent anisotropy. A comparative analysis between the mechanical performance of the desired scaffolds and human bone tissue was conducted, focusing on anisotropic characteristics, as illustrated in Fig. 6. The elastic constants C_{11}, C_{22}, C_{33}, C_{12}, C_{13} and C_{23} of the stiffness matrix were used as comparative indicators. As we know, there are nine independent constants in an orthotropic elastic matrix. Two shear constants in the same direction are strong positive correlation, which also reported in our previous work [16]. Therefore, to concisely exhibited the results, six constants were used as comparative indicators. When compare with the target human bone tissue, the relative errors for the straight pore type I scaffold ranged from 3.44 % to 8.98 %, and for type II, from 1.32 % to 8.49 %, as shown in Figs. 6A and C. After incorporating curved pores, these errors were reduced. For the bending pore type I scaffold, the relative errors decreased to 3.33 % − 6.82 %, while for the bending pore type II, the range was reduced to 1.20 % − 8.20 %, as shown in Figs. 6B and D. These results demonstrate that all novel scaffolds closely replicate the mechanical behavior of human cancellous bone, with the bending pore configurations offering a better match in terms of both elastic moduli and morphological similarity. Furthermore, performance comparisons during the optimization process, summarized in Table 1, revealed that scaffolds using curved components required fewer iterations than those with straight components. This indicates that curved components provided a more favorable initial configuration, thereby enhancing the overall optimization efficiency.

To facilitate a more intuitive comparison of anisotropic behavior between the designed bone scaffold and human bone, the Young's modulus surfaces of both the human cancellous bone and the novel biomimetic scaffolds are illustrated in Fig. 7. The results show that the mechanical performance of the non-periodic biomimetic bone scaffolds closely resembles that of human cancellous bone, thereby demonstrating the effectiveness and feasibility of the proposed design method.

3.3. Permeability of bone scaffolds

The novel bone scaffolds demonstrated excellent permeability, enabling enhanced nutrient transport to surrounding tissues and thereby promoting cell growth. The permeabilities of the scaffolds with straight pore type I and bending pore type I were 3.70×10^{-8} m^2 and 3.61×10^{-8} m^2, respectively, indicating only minimal variation in permeability before and after pore bending. Additionally, variations in porosity led to corresponding changes in permeability. For straight pore type II and bending pore type II, the permeabilities were 1.52×10^{-8} m^2 and 1.47×10^{-8} m^2, respectively. To further demonstrate the superior permeability of the novel non-periodic biomimetic scaffolds, the permeability of a Schwarz P structure was evaluated under the same porosity as the type I scaffold, which can ensure the comparability between the two. The Schwarz P structure exhibited a permeability of 7.95×10^{-9} m^2 which is four times lower than that of the novel scaffolds, as shown in Fig. 8. These results confirm that the permeability of the designed scaffolds was significantly enhanced. Moreover, the fluid streamlines were analyzed to visualize flow behavior. As shown in Fig. 9, the majority of fluid entered and exited through the larger pores, with the flow rate increasing and then decreasing along the pathway, further confirming effective mass transport through the scaffold.

Table 1
Comparison of different components.

Component types	Iteration steps	Objective function value
Straight pore type I	135	0.055
Bending pore type I	73	
Straight pore type II	149	0.033
Bending pore type II	82	

3.4. Manufacturability of bone scaffolds

To validate the manufacturability of the novel non-periodic biomimetic bone scaffolds, samples were fabricated using SLM. The resulting scaffolds exhibited morphological characteristics that were largely consistent with the designed geometries, as illustrated in Fig. 10A, with the internal pores remaining unobstructed and well-formed. Additionally, SEM was performed to examine the surface quality at various magnifications, as shown in Fig. 10B. SEM images captured at 25×, 100 × and 150 × magnifications revealed that the fabricated bone scaffolds possessed high surface quality and demonstrated excellent manufacturability.

4. Discussion

In the present study, novel non-periodic biomimetic bone scaffolds were designed using the MMC method. An explicit boundary evolution technique was employed to optimize the layout of porous bone scaffolds based on the equivalent stiffness method. Within this framework, pores were modeled as slender components and topologically optimized within a defined design domain. Once the optimal component layout was determined, the non-component phases were designated as solid regions, while the component phases represented the pore structures. Two scaffold types were initially obtained with straight pores, designated as type I and type II. To more closely mimic the microstructures of human cancellous bone, the straight components were subsequently transformed into bending components, resulting in bending pore type I and type II scaffolds. The mechanical performance, permeability and manufacturability of these novel bone scaffolds were systematically evaluated. Several key findings emerged from this study, which are summarized below.

First, bone scaffolds with mechanical properties closely matching those of human bone in all directions were successfully designed. This is a critical requirement for bone implants, as osteointegration between bone tissue and the scaffold is significantly enhanced when the scaffold mimics the mechanical behavior of natural bone. The maximum error in the elasticity matrix of the scaffolds with bending pores was found to be lower than that of scaffolds with straight pore, likely due to the improved morphological similarity of the bending pore design to human cancellous bone. Importantly, the issue of stress shielding, a common cause of implant loosening due to bone resorption, may be mitigated by using scaffolds whose average elastic properties closely resemble those of the host bone tissue. By reducing the mismatch in mechanical properties, a larger portion of the applied load can be transmitted through the scaffold to the surrounding bone, promoting more natural load

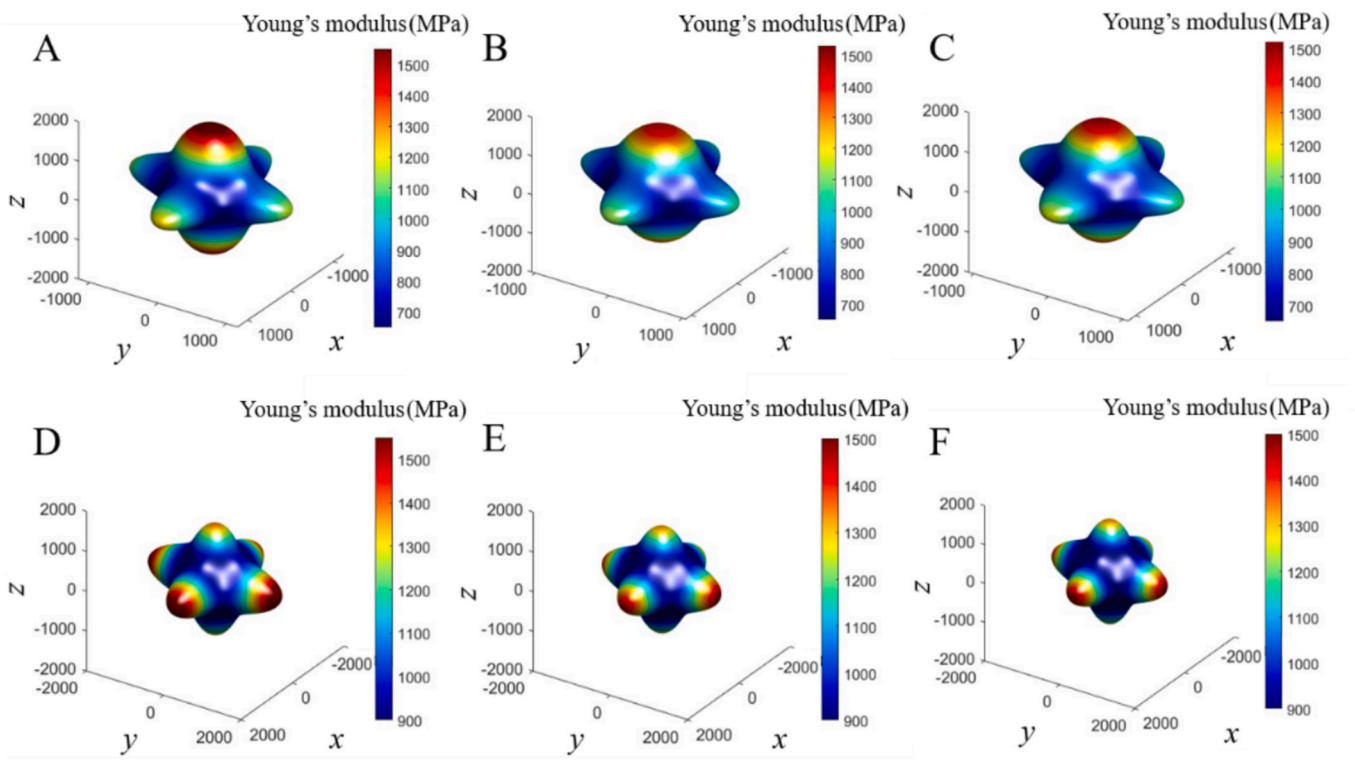

Fig. 7. Young's modulus surfaces of the target bones and corresponding bone scaffolds. (A) Target bone I. (B) Bone scaffold with straight pore type I. (C) Bone scaffold with bending pore type I. (D) Target bone II. (E) Bone scaffold with straight pore type II. (F) Bone scaffold with bending pore type II.

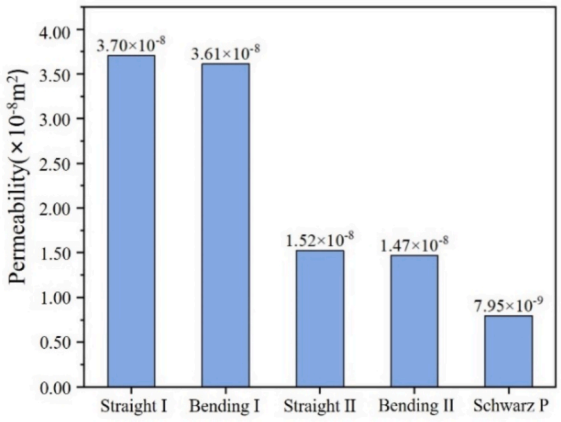

Fig. 8. Permeability results of novel bone scaffolds and Schwarz P structure via CFD simulations.

distribution and reducing the risk of implant failure. Furthermore, the novel scaffold design may be particularly suitable for bone repair in confined anatomical regions due to its geometric adaptability. While previous studies have used topology optimization to address mechanical compatibility, many have overlooked critical factors such as permeability and cellular growth environments [12,13]. Although some researchers have optimized periodic scaffold structures for both maximum stiffness and permeability [37,8], the non-periodic scaffolds developed in this study offer a more biomimetic solution by combining mechanical compatibility with enhanced permeability, thus better supporting bone tissue regeneration.

Second, the novel bone scaffolds demonstrated higher permeability compared to previously reported TPMS-based bone scaffolds. While a slight decrease in permeability was observed after transforming the pores from straight to curved, scaffolds with straight pores were remained slightly more permeable than their curved counterpart at the same porosity. Interestingly, an increase in overall porosity did not always lead to increased permeability – an observation that may seem counterintuitive at first. Upon closer examination, it was found that permeability was primarily influenced by the diameter and orientation of longitudinal pores, which play a dominant role in fluid transport from the top to bottom of the scaffold. Increasing porosity may inadvertently enlarge transverse pores while reducing the diameter of longitudinal pores, ultimately lowering effective permeability. This finding highlights that effective permeability is governed not only by porosity but also by pore connectivity and directional alignment, potentially resulting in anisotropic permeability. Therefore, in order to achieve high permeability, it is more critical to control the diameter of longitudinal pores than to simply increase overall porosity. Although TPMS structures are commonly used in scaffold design for their favorable mechanical and permeability properties [35], novel scaffolds developed in this study achieved approximately four times greater permeability than the Schwarz P-type TPMS structures at equivalent porosity levels. However, it is also essential to ensure that pore size remain within a biologically acceptable range to support bone ingrowth. Human cancellous bone typically features pore sizes ranging from 1.0 μm-1.0 mm, with trabecular plate spacing reaching up to 2.0 mm [38]. In contrast, the novel scaffold with straight pore type I exhibited maximum and minimum pore sizes of 3.05 mm and 0.75 mm, respectively, suggesting that the upper limit of pore size may exceed that of natural bone. This might not be ideal for bone ingrowth due to the excessive pore sizes. Although the large pore sizes of bone scaffold can effectively enhance the capability of mass transport, the nutrient might not normally delivery to bone cells to promote bone ingrowth. Moreover, excessively large pore sizes might compromise the mechanical stability of the bone scaffold when subjected to extreme loads. As such, future work should incorporate pore size constraints into the design process to ensure better compatibility and mechanical stability with microstructure of human

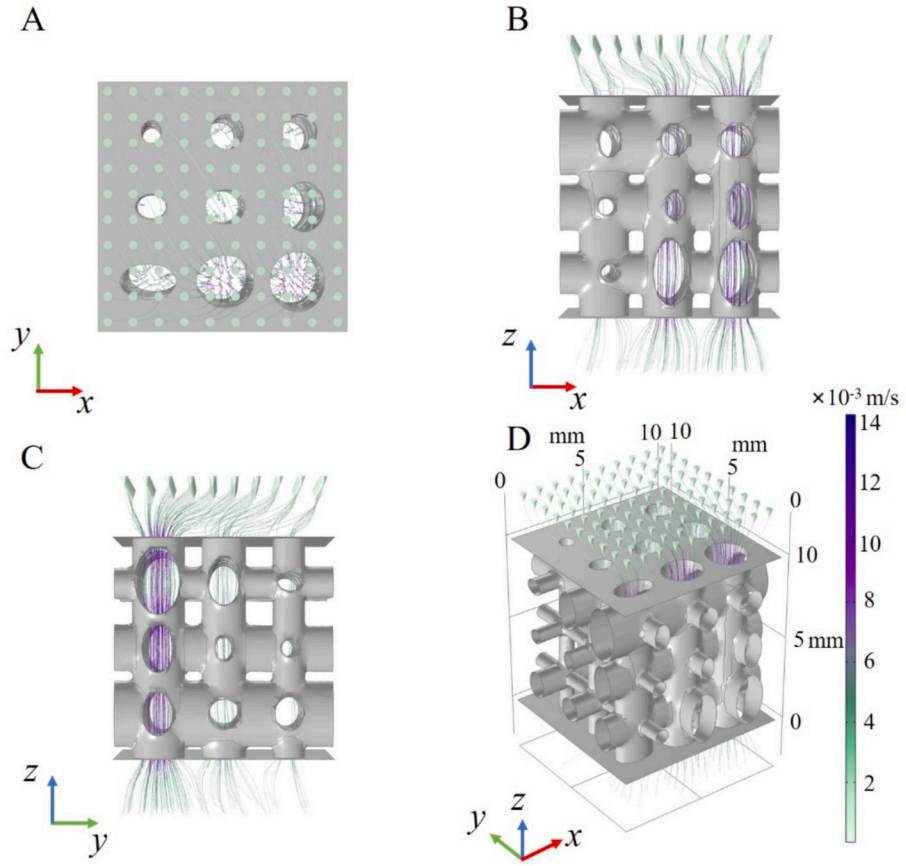

Fig. 9. Distribution of the fluid flow in the bone scaffold with straight pore type I. (A) *x*-*y* plane. (B) *x*-*z* plane. (C) *y*-*z* plane. (D) Axonometric diagram. The color bar represents the fluid velocity.

bone and to promote optimal bone regeneration.

Third, the novel bone scaffolds demonstrate good manufacturability. Using 316L stainless steel powder as the base material, the scaffolds were successfully fabricated via SLM technology with high reproducibility and excellent structural fidelity. The favorable manufacturability of the designed scaffolds highlights their potential for practical application in bone tissue engineering, bridging the gap between computational design and clinical translation.

The results of the present study demonstrated that biomimetic bone scaffolds can be effectively engineered to replicate the diverse mechanical and morphological properties of bones across different anatomical regions. The MMC method exhibited several advantages in the design of porous structures, indicating geometric flexibility and computational efficiency. However, it is important to acknowledge that the outcomes of the optimization process are influenced by the initial design variables. Different initial configurations may lead to distinct scaffold architectures while using consistent initial designs tend to result in more uniform and predictable topologies, thereby enhancing the rationality and reproducibility of scaffold reconstruction. In this study, the pores were also approximated as matrices of tubes with super-elliptic cross-sections, offering a practical geometric abstraction. For more complex structures, applying the MMC design framework can substantially reduce the number of design variables, simplify the optimization process, and improve overall design efficiency. Key advantage of the MMC method include the explicit geometric representation, reduced computational time for FE analysis, and streamlined control over structural features, making it particularly suitable for applications in biomedical engineering. Moreover, the MMC- based approach bears conceptual similarity to inverse homogenization methods in topology optimization [39,40]. While the inverse homogenization framework was originally developed for periodic microstructures, the MMC method extends its utility to non-periodic scaffold designs, offering both efficiency and flexibility in engineering functionally graded biomimetic structures.

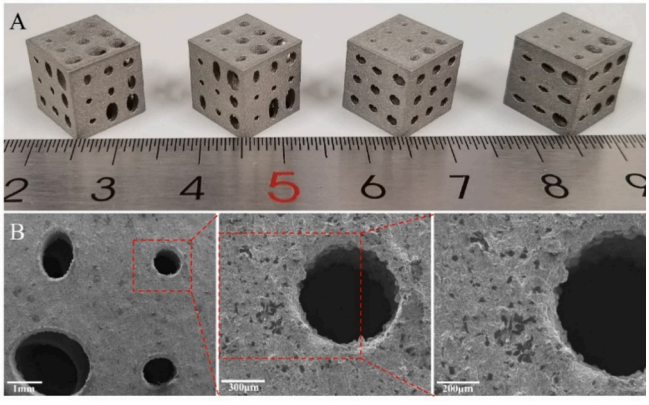

Fig. 10. Additive manufactured samples and SEM images of the novel non-periodic biomimetic bone scaffolds. (A) Fabricated scaffold samples produced using SLM. (B) SEM images of the scaffold surfaces at the magnifications of 25×, 100× and 150×.

Several limitations of the present study should be discussed. First, only the average elastic mechanical properties of the cubic bone scaffolds were investigated. Although the scaffolds demonstrated compatibility with bone tissues, the design of scaffolds with anisotropic mechanical properties more closely resembling those of natural bone, remains an important future direction. The current scaffold designs may

be more suitable for small bone defects, where the defect region can be trimmed into a cuboidal shape and approximately repaired using the proposed scaffold. However, for large bone defects with irregular geometries, cuboidal scaffolds may not be adequate. To address this, future work will focus on using the actual geometry of large bone defects as the design domain, will approximately defined boundary conditions to generate irregularly shaped bone scaffold that conform to the native bone profile. The MMC method offers promising potential for this, as it allows efficient design of complex, irregular scaffold geometries by allowing components to move, deform and overlap. Further exploration is required to establish a framework for designing patient-specific scaffolds that match both the shape and mechanical needs of large bone defects. Additionally, other mechanical characteristics such as fatigue resistance and mechanobiological indices, including wall shear stress [41], should be incorporated in future evaluations to better understand scaffold performance under physiological conditions. Second, although the current study provides comprehensive numerical analyses, experimental validation of the FE simulations and CFD results has not yet been performed. Nonetheless, the simulation methodologies applied here are based on well-established and widely accepted approaches in previous studies [42]. Further research will aim to validate the computational findings through mechanical testing, in vitro and in vivo experiments, cell experiments, and animal studies to assess the biological effectiveness of scaffold designs and their ability to support bone ingrowth. Last but not the least, permeability analysis in this study was limited to a single direction. Given the inherently anisotropic nature of bone and scaffold microstructures, a more detailed evaluation of direction-dependent permeability is critical. It is also very essential to investigate the permeability in transverse direction. Future work should explore the full 3D anisotropic permeability characteristics of the scaffolds to ensure their efficacy in facilitating nutrient transport and vascularization from multiple directions, while also better guiding their utility in load-bearing applications.

5. Conclusion

In this study, the MMC method was employed to design novel non-periodic biomimetic bone scaffolds. The explicit boundary evolution technique was used to optimize the layout of porous structures based on the equivalent stiffness method, with pores modeled as slender components and topologically optimized within a defined design domain. Upon achieving the optimal component configuration, the non-component phases were designated as the solid regions, while the component phases represented the pores. Bone scaffolds with straight pore type I and type II were initially obtained. To better replicate the morphology of human cancellous bone, straight components were subsequently transformed into bending components, yielding bending pore type I and type II scaffolds. All four scaffold types exhibited bone-like mechanical properties, high permeability, and good manufacturability. The key conclusions are summarized as follows:

(1) Elastic properties of the novel scaffolds closely matched those of human cancellous bone, indicating the potential to mitigate stress shielding after implantation.
(2) The permeability of the novel scaffolds was significantly enhanced. At equivalent porosity levels, their permeability exceeded that of TPMS-based scaffolds by more than four times.
(3) The novel scaffolds demonstrated excellent manufacturability, as confirmed by high-quality samples fabricated using SLM.

Overall, the scaffold structures developed using the MMC method show strong potential for applications in medical implants, tissue repair, and broader areas of biomedical engineering, where porous biomaterials must be tailored for specific stiffness and permeability requirements. These designs offer a promising pathway for promoting bone cell growth and regeneration, contributing to the advancement of scaffold-based strategies in bone tissue engineering.

CRediT authorship contribution statement

Hao Wang: Writing – original draft, Methodology, Conceptualization. **Jiongyi Wu:** Methodology, Conceptualization. **Yuhang Chen:** Writing – review & editing, Investigation. **Michael Zhuravkov:** Investigation. **Sergei Bosiakov:** Investigation. **Youwei Zhang:** Writing – review & editing, Resources, Methodology. **Mohammed Rafiq Abdul Kadir:** Writing – review & editing. **Jian Jiang:** Supervision, Investigation. **Yongtao Lyu:** Writing – review & editing, Supervision, Methodology, Funding acquisition, Conceptualization.

Declaration of competing interest

The authors declare that they have no known competing financial interests or personal relationships that could have appeared to influence the work reported in this paper.

Acknowledgement

This work was supported by the National Natural Science Foundation of China (Grant numbers 12572376, 12211530062, 12072066), the National Key R&D Program of China (Grant number 2024YFE0213500), the Fundamental Research Funds for the Central Universities (Grant number DUTIO-ZG-202501, DUT25YG245), and the DUT-BSU Joint Institute Fund (Grant number ICR2303).

Data availability

Data will be made available on request.

References

[1] V. Campana, G. Milano, E. Pagano, et al., Bone substitutes in orthopaedic surgery: from basic science to clinical practice, J. Mater. Sci. - Mater. Med. 25 (10) (2014) 2445–2461.
[2] I.-J. Wallace, S. Worthington, D.-T. Felson, et al., Knee osteoarthritis has doubled in prevalence since the mid-20th century, Proc. Natl. Acad. Sci. 114 (35) (2017) 9332–9336.
[3] A. Chmielewska, D. Dean, The role of stiffness-matching in avoiding stress shielding-induced bone loss and stress concentration-induced skeletal reconstruction device failure, Acta Biomater. 173 (2024) 51–65.
[4] E. Liverani, G. Rogati, S. Pagani, et al., Mechanical interaction between additive-manufactured metal lattice structures and bone in compression: implications for stress shielding of orthopaedic implants, J. Mech. Behav. Biomed. Mater. 121 (2021) 104608.
[5] E. Garner, J. Wu, A.-A. Zadpoor, Multi-objective design optimization of 3D micro-architected implants, Comput. Methods Appl. Mech. Eng. 396 (2022) 115102.
[6] C. Wu, J. Fang, A. Entezari, et al., A time-dependent mechanobiology-based topology optimization to enhance bone growth in tissue scaffolds, J. Biomech. 117 (2021) 110233.
[7] M.-R. Dias, P.-R. Fernandes, J.-M. Guedes, et al., Permeability analysis of scaffolds for bone tissue engineering, J. Biomech. 45 (6) (2012) 938–944.
[8] J.-K. Guest, J.-H. Prévost, Optimizing multifunctional materials: Design of microstructures for maximized stiffness and fluid permeability, Int. J. Solids Struct. 43 (22–23) (2006) 7028–7047.
[9] H.-A. Almeida, P.-J. Bártolo, Design of tissue engineering scaffolds based on hyperbolic surfaces: structural numerical evaluation, Med. Eng. Phys. 36 (8) (2014) 1033–1040.
[10] J. Wieding, A. Wolf, R. Bader, Numerical optimization of open-porous bone scaffold structures to match the elastic properties of human cortical bone, J. Mech. Behav. Biomed. Mater. 37 (2014) 56–68.
[11] D. Kong, Q. Wang, J. Huang, et al., A biomimetic structural material with adjustable mechanical property for bone tissue engineering, Adv. Funct. Mater. 2305412 (2023).
[12] M. Liu, Y. Wang, Q. Wei, et al., Topology optimization for reducing stress shielding in cancellous bone scaffold, Comput. Struct. 288 (2023) 107132.
[13] W. Liu, Y. Zhang, Y. Lyu, et al., Inverse design of anisotropic bone scaffold based on machine learning and regenerative genetic algorithm, Front. Bioeng. Biotechnol. 11 (2023) 1241151.
[14] R. Liu, Y. Chen, Y. Liu, et al., Topological design of a trabecular bone structure with morphology and mechanics control for additive manufacturing, IEEE Access 9 (2021) 11123–11133.

[15] F. Xiao, X. Yin, Geometry models of porous media based on Voronoi tessellations and their porosity-permeability relations, Comput. Math. Appl. 72 (2) (2016) 328–348.
[16] H. Wang, Y. Lyu, J. Jiang, et al., Data-driven inverse design of novel spinodoid bone scaffolds with highly matched mechanical properties in three orthogonal directions, Mater. Des. 251 (2025) 113697.
[17] X. Guo, W. Zhang, W. Zhong, Doing topology optimization explicitly and geometrically—a new moving morphable components based framework, J. Appl. Mech. 81 (8) (2014) 81009.
[18] W. Zhang, J. Yuan, J. Zhang, et al., A new topology optimization approach based on moving Morphable Components (MMC) and the ersatz material model, Struct. Multidiscip. Optim. 53 (6) (2016) 1243–1260.
[19] T. Rochefort-Beaudoin, A. Vadean, J.-F. Gamache, et al., Supervised deep learning for the moving morphable components topology optimization framework, Eng. Appl. Artif. Intel. 123 (2023) 106436.
[20] J. Zhou, G. Zhao, Y. Zeng, et al., A novel topology optimization method of plate structure based on moving morphable components and grid structure, Struct. Multidiscip. Optim. 67 (8) (2024).
[21] Q.-D. Tran, D. Shin, G.-W. Jang, Bayesian optimization-based topology optimization using moving morphable bars for flexible structure design problems, Eng. Struct. 300 (2024) 117103.
[22] S.-A. Catledge, W.-C. Clem, N. Shrikishen, et al., An electrospun triphasic nanofibrous scaffold for bone tissue engineering, Biomed. Mater. (Bristol) 2 (2) (2007) 142–150.
[23] S.-J. Hollister, Porous scaffold design for tissue engineering, Nat. Mater. 4 (7) (2005) 518–524.
[24] W. Chen, X. Huang, Topological design of 3D chiral metamaterials based on couple-stress homogenization, J. Mech. Phys. Solids 131 (2019) 372–386.
[25] P. Xiao, E. Haque, T. Zhang, et al., Can DXA image-based deep learning model predict the anisotropic elastic behavior of trabecular bone? J. Mech. Behav. Biomed. Mater. 124 (2021) 104834.
[26] Y. Lu, Y. Zhu, M. Krause, et al., Evaluation of the capability of the simulated dual energy X-ray absorptiometry-based two-dimensional finite element models for predicting vertebral failure loads, Med. Eng. Phys. 69 (2019) 43–49.
[27] W. Deng, S. Kumar, A. Vallone, et al., AI-enabled materials design of non-periodic 3D architectures with predictable direction-dependent elastic properties, Adv. Mater. 2308149 (2024).
[28] J. Jiang, Y. Huo, X. Peng, et al., Design of novel triply periodic minimal surface (TPMS) bone scaffold with multi-functional pores: lower stress shielding and higher mass transport capacity, Front. Bioeng. Biotechnol. 12 (2024) 1401899.
[29] W. Zhang, D. Li, J. Yuan, et al., A new three-dimensional topology optimization method based on moving morphable components (MMCs), Comput. Mech. 59 (4) (2017) 647–665.
[30] L. Karim, V. Deepak, Role of trabecular microarchitecture in the formation, accumulation, and morphology of microdamage in human cancellous bone, J. Orthop. Res. 29 (11) (2011) 1739–1744.
[31] C.-Y. Lin, N. Kikuchi, S.-J. Hollister, A novel method for biomaterial scaffold internal architecture design to match bone elastic properties with desired porosity, J. Biomech. 37 (5) (2004) 623–636.
[32] S. Zhou, Q. Li, The relation of constant mean curvature surfaces to multiphase composites with extremal thermal conductivity, J. Phys. D Appl. Phys. 40 (19) (2007) 6083–6093.
[33] S. Zhou, Q. Li, Computational design of multi-phase microstructural materials for extremal conductivity, Comput. Mater. Sci 43 (3) (2008) 549–564.
[34] A.-A.-R. Rabiatul, S.-J. Fatihhi, A.-P. Md Saad, et al., Fluid–structure interaction (FSI) modeling of bone marrow through trabecular bone structure under compression, Biomech. Model. Mechanobiol. 20 (2021) 957–968.
[35] T. Pires, J. Santos, R.-B. Ruben, et al., Numerical-experimental analysis of the permeability-porosity relationship in triply periodic minimal surfaces scaffolds, J. Biomech. 117 (2021) 110263.
[36] L. Zhang, B. Song, L. Yang, et al., Tailored mechanical response and mass transport characteristic of selective laser melted porous metallic biomaterials for bone scaffolds, Acta Biomater. 112 (2020) 298–315.
[37] V.J. Challis, J.K. Guest, J.F. Grotowski, et al., Computationally generated cross-property bounds for stiffness and fluid permeability using topology optimization, Int. J. Solids Struct. 49 (2012) 3397–3408.
[38] S. Capuani, Water diffusion in cancellous bone, Microporous Mesoporous Mater. 178 (2013) 34–38.
[39] M. Osanov, J.-K. Guest, Topology optimization for architected materials design, Annu. Rev. Mat. Res. 46 (1) (2016) 211–233.
[40] O. Sigmund, Materials with prescribed constitutive parameters: an inverse homogenization problem, Int. J. Solids Struct. 31 (17) (1994) 2313–2329.
[41] Y. Chen, S. Zhou, J. Cadman, et al., Design of cellular porous biomaterials for wall shear stress criterion, Biotechnol. Bioeng. 107 (4) (2010) 737–746.
[42] S. Ma, Q. Tang, Q. Feng, et al., Mechanical behaviours and mass transport properties of bone-mimicking scaffolds consisted of gyroid structures manufactured using selective laser melting, J. Mech. Behav. Biomed. Mater. 93 (2019) 158–169.